II International Conference on Simulation for Additive Manufacturing - Sim-AM 2019
F. Auricchio, E. Rank, P. Steinmann, S. Kollmannsberger and S. Morganti (Eds)

# BOUNDARY CONDITIONS FOR SIMULATION OF POWDER BED FUSION FOR METALLIC GLASS FORMATION: MEASUREMENTS AND CALIBRATIONS

**J. Lindwall*, C.-J. Hassila†, J. J. Marattukalam+ AND A. Lundbäck***

*Department of Engineering Science and Mathematics
Luleå University of Technology, 971 87 Luleå, Sweden
e-mail: johan.lindwall@ltu.se

+ Department of Engineering Science - Ångström Laboratory
Uppsala University, Box 534, 75121, Uppsala, Sweden

† Department of Physics and Astronomy - Ångström Laboratory
Uppsala University, Box 516, 751 20 Uppsala, Sweden

**Key words:** Computational Methods, Additive Manufacturing, Thermal Simulation, Bulk Metallic Glass

**Abstract.** A finite element model for prediction of the temperature field in the powder bed fusion process is presented and compared to measurements. Accurate temperature predictions at the base plate are essential to accurately predict the formation of crystals in a metallic glass forming material. The temperature measurements were performed by equipping the base plate with thermocouples during manufacturing of a cylinder with the glass forming alloy AMZ4. Boundary conditions for heat losses through the base plate/machine contact interfaces was calibrated to fit the measurements. Additional heat losses was used to account for radiation at the top surface and conduction through the powder bed. An interface boundary condition based on conservation of heat flux was examined to match the heat flow to the machine structure and the temperature predictions was satisfying. Still, temperature predictions with a constant heat transfer coefficient matched the measurements within 1.5$^{o}$C during the entire building process of about 9 hours.

## 1 INTRODUCTION

Additive manufacturing with the powder bed fusion (PBF) process enables rapid solidification which is essential for formation of metallic glass. Metallic glass possesses desirable properties for a variety of applications [1]. Unfortunately, they can be difficult to produce in practical dimensions by traditional manufacturing techniques, such as suction casting, melt pinning etc, where the cooling rate might be too low in the bulk. The amorphous structure can only be achieved when crystallization is bypassed and maintained only if not subjected to temperatures above a critical temperature of crystallization. Thus, the temperature history in the material during the PBF process dictates the amount of amorphous phase and formation of crystalline phases.

During simulation of the PBF process, it becomes critical to accurately predict the temperature field close to the melt pool and also in the surrounding material. The base plate/substrate acts as a heat sink that accumulates heat by conduction. During the melting of each layer, heat is conducted through the built material and the base plate. After a few layers, the overall temperature will rise and affect the temperature gradients and hence the cooling rates of the melt pool. The temperature of the base plate can rise to close to the glass transformation temperature if heat is not transported away. Thus, heat losses by radiation, convection and conduction through contact interfaces to the machine plays an important role in the manufacturing of bulk metallic glasses (BMG) with low crystalline fraction. Chiumenti et al. [2] presented a model to account for the heat losses to the powder bed, but without modelling the powder bed domain. Other studies have applied constant convection coefficients to the solid/powder interface [3, 4].

Many researchers have printed BMGs using a laser heat source in PBF [5]. However, crystals can still be found in the manufactured material, even though it looks amorphous in X-ray diffraction measurements. The crystalline phases have been argued to form as a result of thermal cycling in the heat affected zone [6–11]. When the material is remelted, nuclei will dissolve; otherwise, they become trapped in the amorphous matrix and may grow due to diffusion. Simulations of the process can help us understand the thermal events in critical regions where crystals may form and persist. These types of simulations will offer new insights into the process, and in the long term aid the process development, possibly reducing the crystalline fraction in BMG manufactured via PBF.

This study aims to contribute to thermal simulations of the PBF process for accurate predictions of the temperature field that drives crystallization and devitrification. The work is limited to thermal modelling on the overall process with heat losses to the environment. Contact interfaces are replaced with boundary conditions that are estimated by the temperature measurements.

## 2 EXPERIMENTAL SETUP

A cylinder with a diameter of 10 mm was built on a cylindrical base plate with an EOS M100 system. The layer thickness was 20 $\mu$m and the total build height was 60 mm, resulting in a total of 3000 layers. The cylinder was centred on the build plate to ensure rotational symmetry. The diameter and thickness of the base plate was 100 and 21.4 mm respectively. Furthermore, the build plate was prepared with three holes on the bottom side of the plate into which type-K thermocouples were inserted. The holes were drilled to a depth of 16.4 mm, leaving 5mm of material to the surface of the plate. One hole was place in the central position of the plate, i.e., right below where the BMG cylinder was to be built. The other two holes were placed 17.5 mm and 35.0 mm from the central position respectively, as shown in Figure 1. The laser power was 80 W with a scanning speed of 2000 mm/s and a hatch distance of 100 $\mu$m. Each layer was scanned twice with an angular rotation of 67$^{o}$. The process parameters are sumarized in Table 1.

The temperature response was measured during the entire building process (about 9 hours)

[1]Estimated value used in simulations

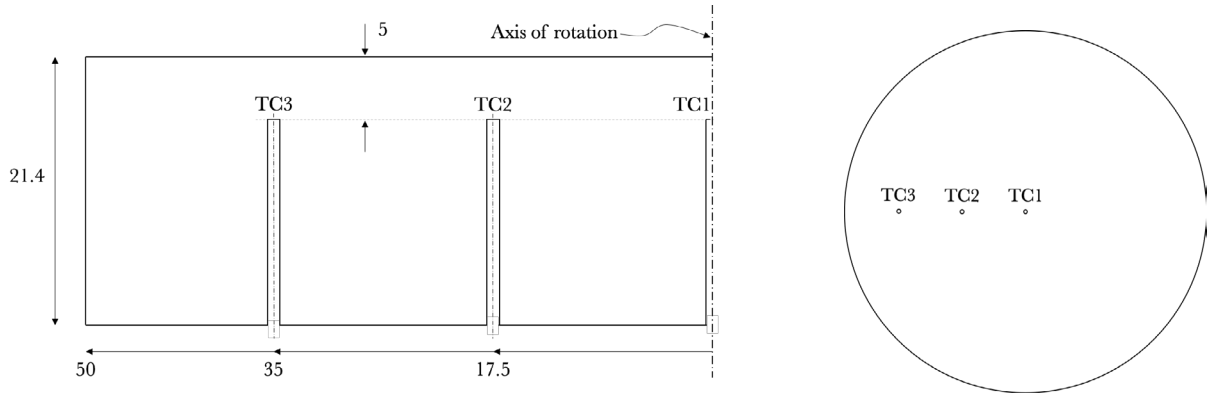


(a) Side view (b) Top view

Figure 1: Measurements of base plate (unit mm) and locations of thermocouples (TC).

Table 1: Process parameters

| | | |
|---|---|---|
| Laser power | 80 | W |
| Scan speed | 2000 | mm/s |
| Layer thickness | 20 | $\mu$m |
| Laser efficiency [1] | 40 | % |
| Hatch distance | 100 | $\mu$m |
| Penetration depth | 80 | $\mu$m |

as well as during the time it took for the machine to reach ambient temperatures, a total of 15 hours, as presented in Figure 2. From the beginning of the build, Figure 2b, it was possible to determine the time between each successive layer to 10 seconds. It was also found that every 10th layer used an additional pause time of 2.65 seconds, possibly for referencing of the laser. During this extra pause, the base plate is given additional time to dissipate heat and results in lowering of the temperature of the whole system.

## 3 MODELLING APPROACH

The manufacturing process was reduced to a two dimensional axisymmetric modelling domain, including the base plate and the cylinder of the printed material, Figure 3. All elements that represent the build material were first subdivided in three levels and then deactivated during the initiation of the simulation. Each sub-element then reached the thickness of one layer, i.e., 20 $\mu$m. These sub-elements were then activated in a layer-by-layer fashion and later on unrefined to restore the parent elements.

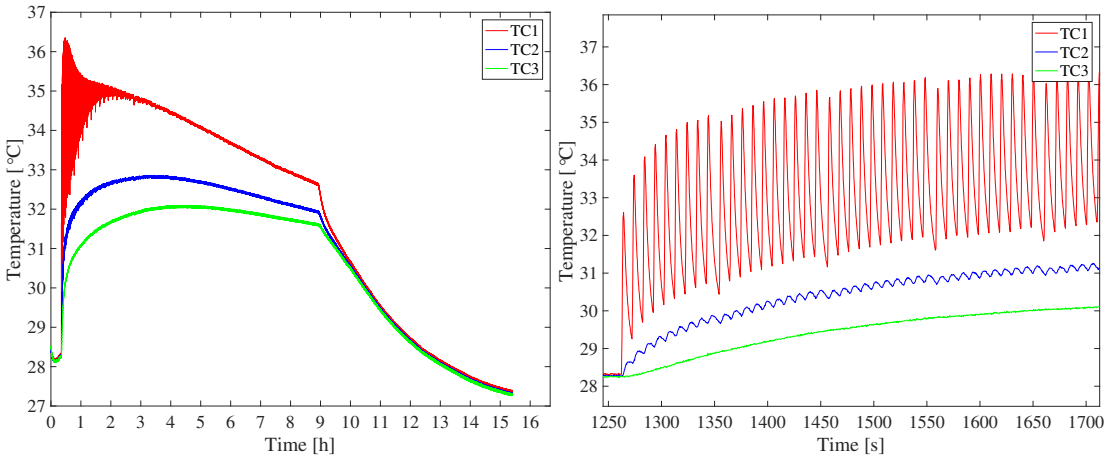


(a) Whole range with gas flooding, printing and cooling

(b) Beginning of printing

Figure 2: Temperature response at the three thermocouples in the base plate during printing with 80 W.

### 3.1 Heat input

The heat input was modelled by a volumetric heat flux acting on the entire layer simultaneously. The heat was distributed using a Gaussian expression according to Equation (1), as presented previously by [11],

$$q(z) = \frac{2\sqrt{3}\eta Q}{\sqrt{\pi}ch^2} e^{\frac{-3z^2}{c^2}} \tag{1}$$

where $Q$ is the laser powder, $\eta$ the efficiency/absorption fraction of the laser, $c$ the penetration depth and $h$ the hatch spacing. The heat input acted during a characteristic time of $t_{heat} = h/v$ where $v$ is the scanning speed. The heating procedure in the simulation used two heating sequences for each layer and was modelled with two heating load cases with a dwell time in between. The dwell time corresponds to the scanning time of an entire layer in the PBF experiment.

### 3.2 Heat losses

Heat dissipate from the heated area and conducts through the built material and base plate and further on to the powder bed and to the machine. Described in this section are the boundary conditions for heat losses into the powder bed, the atmosphere and to the printer.

#### 3.2.1 Powder bed

The interaction between the cylinder and the powder bed was represented by a face film boundary condition with a coefficient, $h_{powder}$, acting on all surfaces facing the powder bed,

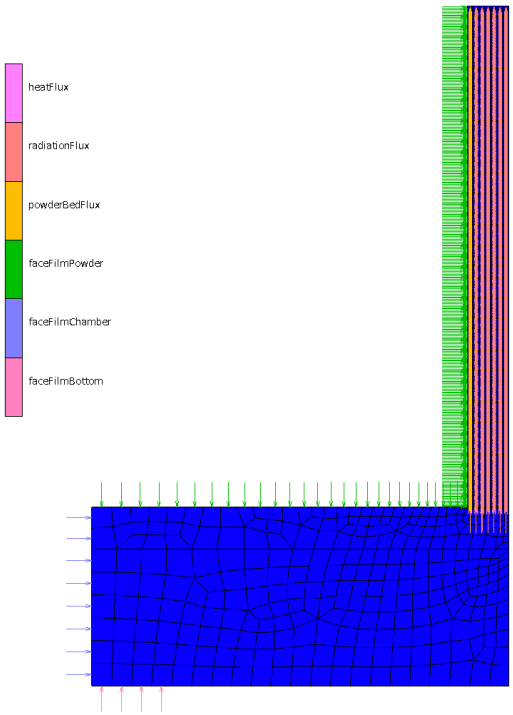


Figure 3: Two dimensional axisymmetric modelling domain.

as shown by the boundary condition `faceFilmPowder` in Figure 3. During the course of the simulation/build, as the height of the cylinder increased, the active face film area continuously increased as more layers were activated. In the beginning of the printing process, the cross-sectional area of the printed component is much larger than the circumferential area. This combined with a much larger conductivity in the solid material compared to the powder bed results in a heat flux that is dominated by thermal conductivity towards the base plate. On the other hand, as the build progresses, the circumferential area becomes much larger than the cross sectional area (which stays constant) and heat flux towards the powder bed can instead be the dominating heat loss, provided that the powder bed conducts heat and continues to lose heat to the environment. These arguments can explain why the temperature curves in Figure 2 have a peak temperature and then starts to decline, i.e., after the peak temperature, the heat flux towards the thermocouples in the base plate is continuously reduced.

### 3.2.2 Free surface

The top surface of the scanned area was subjected to heat losses by radiation. This boundary condition was updated every time a new layer was activated to only act on the top surface of the cylinder. Heat loss by convection from the free surface was neglected as the protective argon gas is a very poor heat conductor and the gas was circulated.

### 3.2.3 Machine

During the printing process, the base plate is held in place by a vacuum. This attachment results in a contact pressure in the outer rim of the base plate and offers a possibility for heat transport towards the machine. This contact was modelled using a face film with a film coefficient, $h_{bottom}$ acting on the edges indicated by `faceFilmBottom` in Figure 3.

The radial contact to the machine is non or very low as there is a small gap between the base plate and the chamber wall such that the build plate can move freely in the vertical direction. Thus, heat transport through this interface was assumed to be very low and a face film coefficient on `faceFilmChamber` was set to zero.

## 4 CALIBRATION TO EXPERIMENTS

The temperature was predicted at the locations that corresponds to the positions of the thermocouples. The boundary conditions in the FE-model was calibrated to fit the temperature measurements on the base plate.

### 4.1 Bottom face film

The face film coefficient at the bottom of the base plate was estimated by conservation of heat flux through the base plate and the interface to the machine. The rate of heat flow between TC2 and TC3, $J$, can be estimated by the thermal conductivity of the material, a cross-sectional area, $S$ and the temperature gradient.

$$J = -kS\frac{\Delta T}{x} \tag{2}$$

In this expression, $k$ is the thermal conductivity of Titanium, hence a fixed value of 21.8 W/mK was used, corresponding to the conductivity at 32°C. The area was selected as indicated in Figure 4a located at the mean radius between TC2 and TC3. The temperature gradient was computed by the measured temperature difference between TC2 and TC3 and the fixed distance of $x = 17.5$ mm. The rate of heat transfer was then assumed to equal the heat transfer through the contact interface, $S_I$, that covers the outer 10 mm of the base plate as indicated by the highlighted area in Figure 4b.

$$J = h\Delta T_I S_I \tag{3}$$

Here, $h$ is the film coefficient (W/m$^2$K), $\Delta T_I$ the temperature difference between the base plate and the machine over the interface. Thus, equating Equations (2) and (3) gives:

$$h = \frac{kS\Delta T}{x\Delta T_I S_I}. \tag{4}$$

The resulting film coefficient was then computed by letting $\Delta T_I$ be the difference between an estimated temperature at the base plate, extrapolated by TC2 and TC3, and the surrounding temperature of 27°C. The computed film coefficient and an estimated function is presented in Figure 5.

$$h = a \cdot t^b + c \tag{5}$$

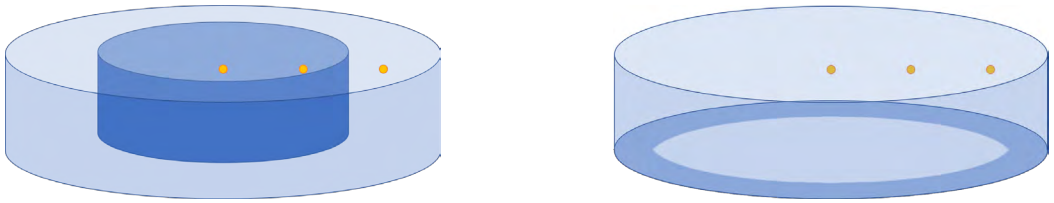

(a) Heat flux through base plate from TC2 to TC3.

(b) Heat flux through contact interface between base plate and machine.

Figure 4: Conservation of heat flux through the highlighted areas in the base plate is used to estimate the film coefficient. Dots indicates the locations of thermocouples.

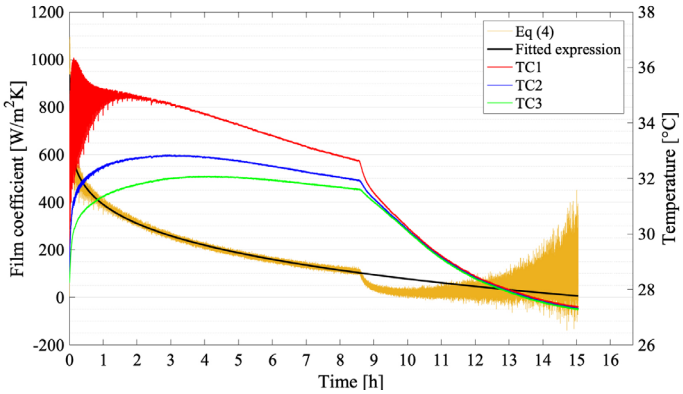


Figure 5: Estimated film coefficient by temperature difference at TC2 and TC3 and fitted with a simple power law equation $h = a \times t^b + c$ with $a = -109.6$, $b = 0.1964$ and $c = 938.2$.

## 5 RESULTS & DISCUSSION

The temperature history at the locations that corresponds to the positions of the thermocouples was computed during the full time of the experiment. The result with a varying film coefficient over time is shown in Figure 6a. The predicted temperature is a few degrees lower than the measured during the first half of the built. During the end on the other hand, the predicted temperature have continued to increase above the measured temperatures. The continuously decreasing heat transfer coefficient allowed the thermal energy to be stored in the base plate.

The results were compared to a model with a fixed heat transfer coefficient of 150 W/m$^2$K at the bottom of the base plate. Then, the predicted temperatures became comparable to the measured, as shown in Figure 6b. A lower heat transfer in the beginning of the simulation resulted in higher temperatures in the base plate compared to the PBF measurements and previous simulation. The predicted temperature then decreased and became 1-1.5 degrees lower than the measured temperature at the end of the 9 hours built time.

During the cooling sequence, when the cylinder is completed, the computed temperature dropped more quickly compared to the PBF measurements. The slow cooling indicates that the surrounding environment and machine have been heated and stores most of the transferred heat.

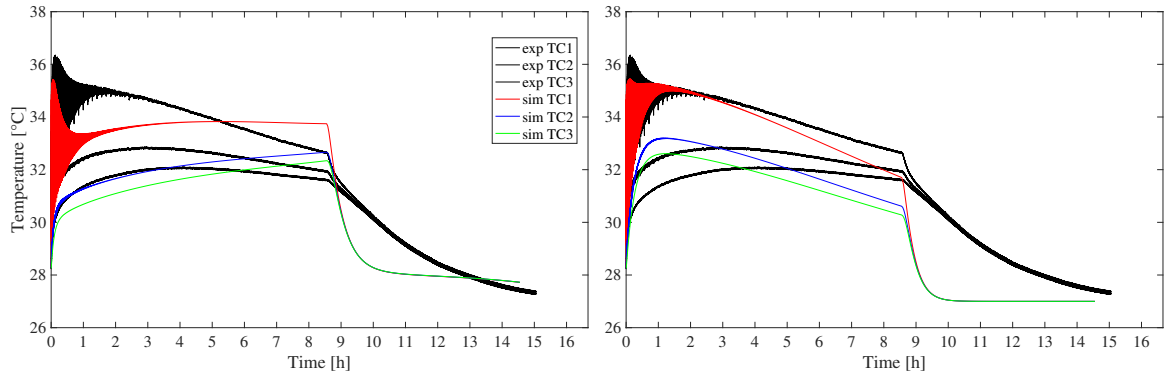


(a) (b)

Figure 6: Temperature prediction with a film coefficient that is; (a), time dependent according to fitted exponential function and (b) a constant value.

Thus, accurate predictions of the temperature after build completion should be done with an extended model, including the mass of the machine.

## 6 CONCLUSION

This study elaborates on the boundary conditions for heat losses in the PBF process for accurate predictions of the temperature field in the base plate while printing a bulk metallic glass. Accurate predictions of the temperature field in the base plate becomes necessary when predicting the microstructure in the manufactured component. Lack of boundary conditions for heat losses would lead to increasing temperatures in the base plate. Increasing temperatures would favor crystallization and result in in-accurate phase predictions.

This work uses measured temperatures in the base plate for calibration of boundary conditions when manufacturing a 60 mm high cylinder. A time varying heat transfer coefficient based on the temperature measurements was proposed to define the heat losses at the machine/base plate contact interface. At the beginning of the build, the heat transfer coefficient is high due to the temperature difference at TC2 and TC3 together with a small temperature difference between the base plate and machine material. As the build progresses, the temperature difference between the thermocouples reduces and the temperature of the base plate increases, which results in a reduced heat transfer coefficient. Satisfying predictions was achieved using this boundary condition together with a fixed heat transfer coefficient in the powder interface. Yet, the time varying heat transfer provided to much cooling at the beginning of the build that indicated an overestimation of the heat transfer coefficient through the interface. Instead, good predictions within 1.5°C was achieved during the roughly 9 hours built by choosing a constant heat transfer coefficient at the contact interface.

## ACKNOWLEDGEMENT

This research was supported by the Swedish Foundation for Strategic Research, SSF, project "Development of Process and Material in Additive Manufacturing", Reference number GMT14-0048.

## References

[1] M. M. Khan, A. Nemati, Z. U. Rahman, U. H. Shah, H. Asgar, and W. Haider. "Recent Advancements in Bulk Metallic Glasses and Their Applications: A Review". *Critical Reviews in Solid State and Materials Sciences* 43.3 (2018), pp. 233–268.

[2] M. Chiumenti, E. Neiva, E. Salsi, M. Cervera, S. Badia, J. Moya, Z. Chen, C. Lee, and C. Davies. "Numerical modelling and experimental validation in Selective Laser Melting". *Additive Manufacturing* 18 (Dec. 2017), pp. 171–185.

[3] Y. Z. B and G. Guillemot. "Macroscopic Finite Element Thermal Modelling of Selective Laser Melting for IN718 Real Part Geometries". *Industrializing Additive Manufacturing - Proceedings of Additive Manufacturing in Products and Applications - AMPA2017* September (2017).

[4] E. R. Denlinger, M. Gouge, J. Irwin, and P. Michaleris. "Thermomechanical model development and in situ experimental validation of the Laser Powder-Bed Fusion Process". *Additive Manufacturing* 16 (2017), pp. 73–80.

[5] E. Williams and N. Lavery. "Laser processing of bulk metallic glass: A review". *Journal of Materials Processing Technology* 247.March (2017), pp. 73–91.

[6] G. Yang, X. Lin, F. Liu, Q. Hu, L. Ma, J. Li, and W. Huang. "Laser solid forming Zr-based bulk metallic glass". *Intermetallics* 22 (2012), pp. 110–115.

[7] B. Chen, T. Shi, M. Li, C. Wen, and G. Liao. "Crystallization of $Zr_{55}Cu_{30}Al_{10}Ni_5$ Bulk metallic glass in laser welding: Simulation and experiment". *Advanced Engineering Materials* 17.4 (2015), pp. 483–490.

[8] Y. Zhang, X. Lin, L. Wang, L. Wei, F. Liu, and W. Huang. "Microstructural analysis of $Zr_{55}Cu_{30}Al_{10}Ni_5$ bulk metallic glasses by laser surface remelting and laser solid forming". *Intermetallics* 66 (2015), pp. 22–30.

[9] Y. Lu, H. Zhang, H. Li, H. Xu, G. Huang, Z. Qin, and X. Lu. "Crystallization prediction on laser three-dimensional printing of Zr-based bulk metallic glass". *Journal of Non-Crystalline Solids* 461 (2017), pp. 12–17.

[10] Y. Shen, Y. Li, and H.-L. Tsai. "Evolution of crystalline phase during laser processing of Zr-based metallic glass". *Journal of Non-Crystalline Solids* 481 (Feb. 2018), pp. 299–305.

[11] J. Lindwall, V. Pacheco, M. Sahlberg, A. Lundbäck, and L. E. Lindgren. "Thermal simulation and phase modeling of bulk metallic glass in the powder bed fusion process". *Additive Manufacturing* 27.October 2018 (2019), pp. 345–352.